ADVANCED FUNCTIONAL MATERIALS
www.afm-journal.de

Achieving High *zT* with Carbon Nanotube/Conjugated Microporous Polymer Thermoelectric Nanohybrids by Meticulous Molecular Geometry Design

Meng-Hao Lin, Mohamed Gamal Mohamed, Chih-Jung Lin, Yu-Jane Sheng, Shiao-Wei Kuo, and Cheng-Liang Liu**

Conjugated microporous polymers (CMPs) are characterized by high physical and chemical stabilities along with low thermal conductivities due to their conjugated microporous frameworks, making them promising candidates for thermoelectric application. However, the advancement of CMPs within the thermoelectric field is considerably hampered by their inadequate electrical conductivity and unfavorable processability. Herein, highly-conducting carbon nanotubes (CNTs) are dispersed in two solvents (1,2-dichlorobenzene and *N*-methyl-2-pyrrolidone) to fabricate p- and n-type CNT/CMP nanohybrids. Additionally, two unique CMPs are synthesized to elucidate the impacts of the chemical structures and pore architectures on the thermoelectric properties of the nanohybrids. Finally, due to the differing steric hindrance effects of the two CMPs, the thermoelectric performance can be tuned under varying circumstances. The synergetic effects of low thermal conductivity and efficient dispersion capability of the CMPs yield optimized figure of merit (*zT*) values of 0.053 and 0.13 at 303 K for the p- and n-type thermoelectric nanohybrids, respectively. This investigation presents an alternative approach to building high *zT* p- and n-type thermoelectric CNT/CMP nanohybrids operating near ambient temperature via the solvent doping effect and chemical structure design of the CMPs, thereby establishing CMP-based materials as promising candidates for thermoelectric application.

1. Introduction

Due to the rapid global growth of industry, heightened concerns over the energy crisis and environmental pollution have spurred the utilization of renewable energy and the advancement of eco-friendly energy materials. Notably, thermoelectric materials that are capable of directly converting waste heat into electricity have great promise for meeting future energy demands.[1] The efficacy of energy conversion in these materials is commonly assessed through the dimensionless figure of merit (zT), given by:

$$zT = S^2\sigma T\kappa^{-1} \quad (1)$$

where S is the Seebeck coefficient, σ is the electrical conductivity, κ is the thermal conductivity, and T is the working temperature.[2] Accordingly, optimizing the zT necessitates the concurrent enhancement of the electrical conductivity and Seebeck coefficient and mitigation of the thermal conductivity. However, achieving this optimization presents a dilemma, as these thermoelectric parameters are intrinsically interrelated.[3] Consequently, extensive efforts have been directed towards mitigating this trade-off and enhancing the thermoelectric properties. In particular, the integration of organic/inorganic nanohybrids has emerged as a promising strategy for increasing zT values, especially for applications that require flexibility and wearability.[4]

M.-H. Lin, C.-L. Liu
Department of Materials Science and Engineering
National Taiwan University
Taipei 10617, Taiwan
E-mail: liucl@ntu.edu.tw

M. G. Mohamed, S.-W. Kuo
Department of Materials and Optoelectronic Science and Center for Functional Polymers and Supramolecular Materials
National Sun Yat-Sen University
Kaohsiung 80424, Taiwan
E-mail: kuosw@faculty.nsysu.edu.tw

C.-J. Lin, Y.-J. Sheng
Department of Chemical Engineering
National Taiwan University
Taipei 10617, Taiwan

C.-L. Liu
Advanced Research Center for Green Materials Science and Technology
National Taiwan University
Taipei 10617, Taiwan

The ORCID identification number(s) for the author(s) of this article can be found under https://doi.org/10.1002/adfm.202406165

DOI: 10.1002/adfm.202406165

By combining organic and inorganic constituents, synergistic advantages can be harnessed to offset individual shortcomings, thereby yielding marked improvements in the thermoelectric characteristics.

Recently, the incorporation of porosity into materials to induce the phonon scattering phenomenon has been recognized as an effective method for diminishing the thermal conductivity and enhancing the zT value.[5] Porous organic polymers (POPs), which are generally connected by covalent bonds, have attracted considerable attention as next-generation functional materials.[6] These encompass distinct variants such as hyper-crosslinked polymers (HCPs),[7] covalent organic frameworks (COFs),[8] and conjugated microporous polymers (CMPs),[9] each of which are endowed with tailored properties to suit diverse applications. Among these, the CMPs are distinct from other porous polymers due to their particular π-conjugated frameworks and microporous characteristics. Moreover, the CMPs have attracted significant interest due to advantages such as excellent physical and chemical stability, high specific surface areas, and tunable π-conjugated porous architectures.[10] Furthermore, the CMPs have the potential to be synthesized on a large scale by using renewable raw materials, at low temperatures, and with minimal waste.[11] In comparison to conventional porous counterparts such as metal-organic frameworks (MOFs), CMPs exhibit unique properties, including robust high-temperature endurance, large pore sizes, permanent nanopores, chemical inertness, amorphous characteristics, and enhanced electrical conductivity.[12] The amorphous characteristic will endow CMP lower thermal conductivity than crystalline porous materials and the fully conjugated framework will help enhance their charge transfer capabilities. These distinctive features make the CMPs inherently advantageous for future thermoelectric applications, offering a competitive edge over MOFs. Nonetheless, a present limitation hindering the widespread adoption of CMPs in thermoelectric contexts pertains to their relatively low electrical conductivity. As a result, combining conducting carbon materials such as carbon nanotubes (CNTs) and graphene with CMPs is regarded as a potential strategy for enhancing their electrical conductivity and improving their thermoelectric performance.[13]

Single-walled CNTs are renowned for their outstanding electrical characteristics, especially their high electrical conductivity (hundreds to thousands of S cm^{-1}). Therefore, they have been extensively integrated into thermoelectric hybrid systems.[4c] However, challenges associated with CNT dispersion and interfacial contact have been regarded as crucial aspects in improving thermoelectric performance.[14] Various surface modifications have been made to overcome the issue of severe physical entanglement and improve the CNT dispersion. For example, although covalently functionalized CNTs are effective in improving dispersion, their use may lead to partial degradation of the extended π-conjugated network, thereby diminishing the electrical conductivity. By contrast, noncovalent modifications offer a promising avenue for preserving the inherent π-electronic characteristics of the CNTs.[15] For instance, the use of π-conjugated polymers facilitates the effective dispersion of CNTs due to the interactions between the polymers' π-rings and the CNTs.[16] Thus, the CMPs and CNTs are able to complement each other in thermoelectric applications, with the highly conjugated CMP framework helping to facilitate CNT dispersion in various solvents and potentially mitigating the high thermal conductivity of the CNTs, while the CNTs serve to enhance the electrical conductivity within the nanohybrid system.[17] Furthermore, the robust mechanical properties inherent to the CNT network contribute to the overall flexibility of the nanohybrid, even without the need for other additives.[13]

In addition, the control of polarity in thermoelectric materials is vital for the development of practical thermoelectric generators (TEGs).[18] In this context, the CNTs inherently act as p-type materials due to oxygen molecule doping from the surrounding environment.[19] However, CNTs are surface-sensitive materials, and modifying the solvent environment can easily influence the charge-carrier type in the CNTs. Specifically, the utilization of polar protic solvents (e.g., alcohols) and nonpolar or weakly polar solvents (e.g., chlorinated compounds) typically yields a positive Seebeck coefficient, whereas polar aprotic solvents such as nitrogen-containing compounds or carbonyl compounds tend to induce a negative Seebeck coefficient.[20] This intriguing phenomenon underscores the potential for achieving both p- and n-type characteristics in CNTs through judicious selection of the dispersion solvent, thereby enabling tailored control over the thermoelectric polarity.

In the present study, CNTs are used to enhance the electrical conductivity and improve the mechanical properties of CMPs. Furthermore, the selection of solvents, specifically 1,2-dichlorobenzene (DCB) and N-methyl-2-pyrrolidone (NMP), is strategically utilized to disperse the CNT solution, thereby realizing p- and n-type thermoelectric nanohybrids. To investigate the relationship between the structural characteristics of the CMPs and their thermoelectric behaviors, two distinct CMPs are synthesized from a common pyrene (Py) core, and attached by triple bond (T) with different ligands (namely, anthracene (A) or thianthrene (T)), to obtain the samples designated as PyT-A and PyT-T, respectively. Further, the weight ratios of the CNT/CMP nanohybrids are systematically altered to achieve the desired thermoelectric properties. The unique steric hindrance effects inherent to the two CMPs afford flexibility in modulating the doping level through dispersion solvents and weight ratios, consequently fine-tuning the thermoelectric performance of the nanohybrids. The highest recorded zT values obtained in this work are 0.053 and 0.13 for the respective p-type CNT/PyT-A nanohybrid dispersed in DCB and the n-type CNT/PyT-T nanohybrid dispersed in NMP. Furthermore, these optimized p- and n-type nanohybrids demonstrate utility in constructing a flexible TEG with a maximum open-circuit voltage (V_{oc}) of 15.6 mV and a maximum power output (P_{max}) of 196.6 nW. This study not only introduces a methodology for achieving high zT p- and n-type thermoelectric nanohybrids via precise control of the molecular geometry but also presents the first CMP-based thermoelectric applications.

2. Results and Discussion

2.1. Synthesis of the CMP and Fabrication of the CNT/CMP Nanohybrids

The chemical structure design approach of the CMPs investigated in this study is shown in **Figure 1a**. Two distinct CMPs were synthesized via the Sonogashira coupling reaction of tetraethynylpyrene (Py-T) with 9,10-dibromoanthracene

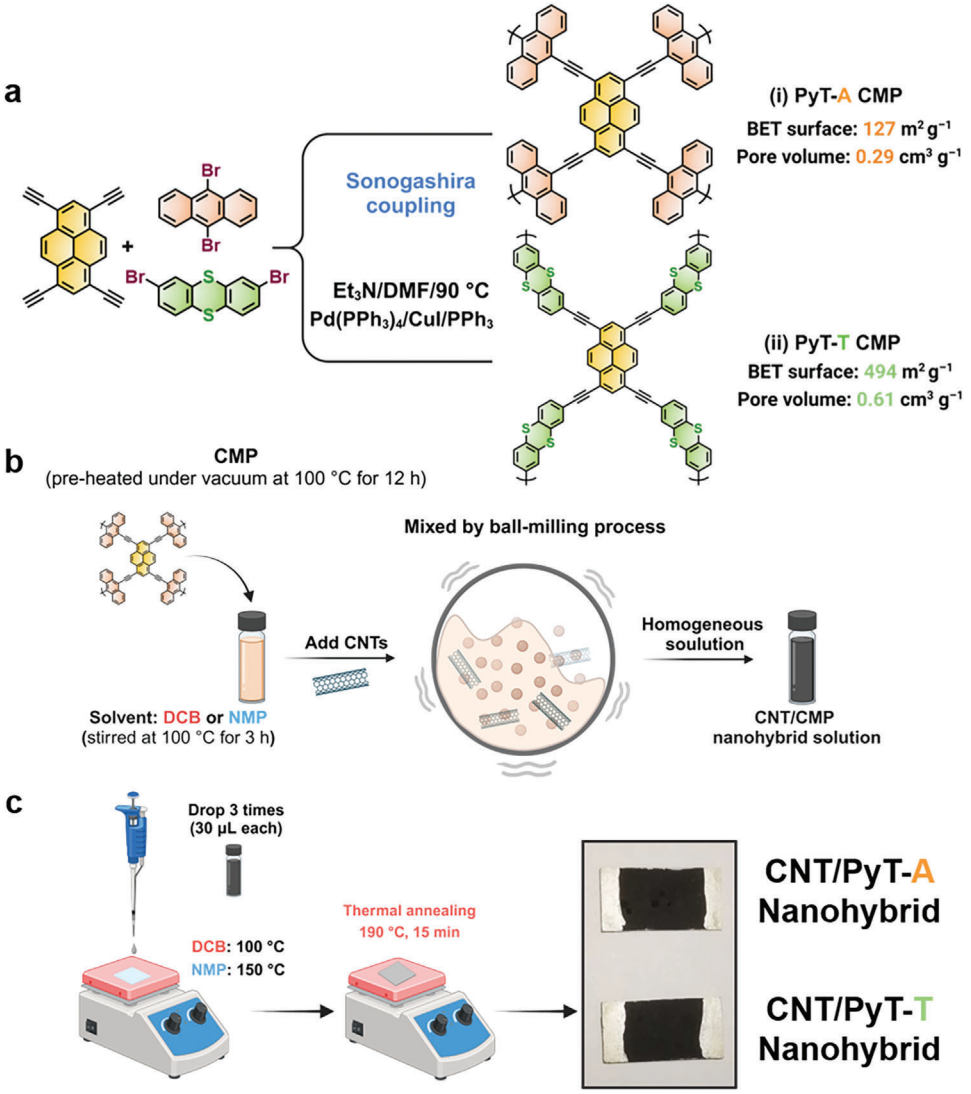

Figure 1. a) Schematic synthesis pathways of PyT-A and PyT-T CMP. b) Preparation process of CNT/CMP nanohybrid solution. c) Procedure for the fabrication steps of the CNT/CMP nanohybrid thin films.

(An—Br_2) to obtain PyT-A, or with 2,8-dibromothianthrene (Th—Br_2) to obtain PyT-T, using dimethyl formamide/triethylamine (DMF/Et_3N) as the solvent and tetrakis(triphenylphosphine)palladium(0) ($Pd(PPh_3)_4$) as the catalyst. The detailed synthesis procedures of the CMPs and their precursors are provided in the Experimental Section and Supporting Information (Figures S1—S6, Supporting Information). In addition, a schematic representation of the thermoelectric nanohybrid fabrication process is provided in Figure 1b,c, with additional details in the Supporting Information. Briefly, in nanohybrid preparation process, a fixed weight of 2 mg for the CNT component will be added to each nanohybrid. To achieve different nanohybrid compositions, the amount of CMP was adjusted accordingly. For instance, in the case of CNT2/CMP1, the weight of CMP was set at 1 mg, resulting in a CMP weight ratio of ≈33%. After weighting suitable amounts of CMPs and CNTs, they were introduced to the dispersion solvents (DCB and NMP), followed by ball-milling to produce a homogeneous solution. The CNT/CMP nanohybrid thin films were then obtained by drop-casting followed by an appropriate thermal annealing method. The resulting nanohybrid thin films are denoted hereafter as CNTx/CMPy, where x and y represent the relative weight ratios of the CNTs and CMPs.

The room-temperature Fourier transform infrared (FTIR) spectra of the PyT-A and PyT-T CMPs are provided in Figure S7, (Supporting Information), where the typical absorption signals associated with the C═C aromatic groups (1590–1630 cm^{-1}), terminal alkynyl groups (2200 cm^{-1}), and C—H aromatic groups (3030–3055 cm^{-1}) are observed. Notably, the disappearance of the absorption band corresponding to the C—Br group after the reaction indicates the successful formation of cross-linked networks.[21] For further characterization, the solid-state ^{13}C NMR spectra of the CMPs are given in Figure S8 (Supporting Information). There, the typical carbon signals associated with phenyl groups are observed in the range of 129.34–142.61 ppm for all samples, along with resonance peaks at 77.59–80.26 ppm

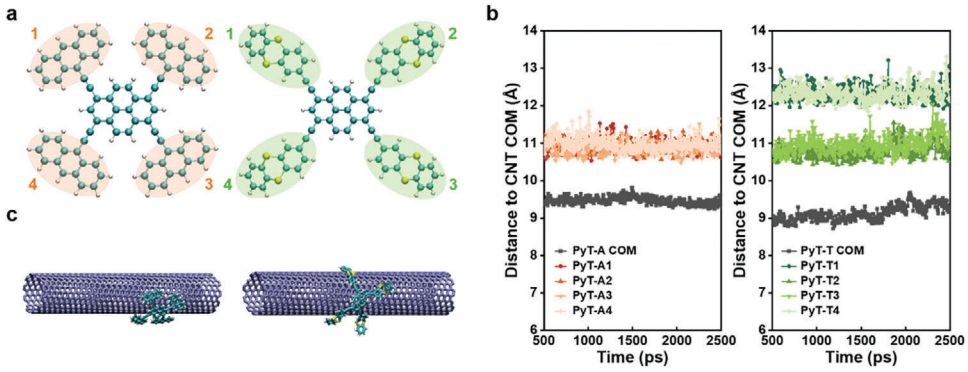

Figure 2. a) Optimized molecular structure of PyT-A and PyT-T utilized for MD simulation, with four ligands marked with a number to evaluate the distance between CNT and CMP. b) Analysis of distance between CMP and COM of CNT. c) Comparison illustration of the different wrapping behavior of CNT/PyT-A and CNT/PyT-T.

due to the alkyne groups. Moreover, the thermal stabilities of the PyT-A and PyT-T are indicated by the thermogravimetric analysis (TGA) results in Figure S9 (Supporting Information), with weight residues of 69% and 70%, respectively, at 800 °C, and degradation temperatures (T_d) of 321.4 °C and 346.0 °C for the PyT-A and PyT-T, respectively, indicating a high level of thermal stability for both CMPs.

As depicted in Figure 1a, the CMPs investigated herein share a common pyrene (Py) core but are linked by triple bond (T) to different ligands (anthracenes (A) or thianthrenes (T)), thus suggesting potential variations in molecular shapes and pore behaviors. Hence, the pore structures of the PyT-A and PyT-T samples are revealed by the Brunauer-Emmett-Teller (BET) results in Figures S10 and S11 (Supporting Information). Here, the BET surface areas of the PyT-A and PyT-T are 127 and 494 $m^2 g^{-1}$, respectively, and the corresponding pore volumes are 0.29 and 0.61 $cm^3 g^{-1}$, respectively. The rationale behind the superior pore capacity and surface area of the PyT-T is elucidated by the density functional theory (DFT) calculations were performed at the B3LYP/6-31G(d) level using the Gaussian 09 W software to investigate the relationship between molecular structure and pore geometry. The results, depicted in Figure S12 (Supporting Information), illustrate front and side views of the PyT-A and PyT-T structures, along with the corresponding highest occupied molecular orbital (HOMO) and lowest unoccupied molecular orbital (LUMO). Analysis of their molecular structures reveals that the PyT-A possesses a highly planar configuration, which can be attributed to its well-conjugated feature and all-carbon structure. Conversely, while the PyT-T maintains a highly conjugated structure, the introduction of sulfur heteroatoms significantly distorts the molecular structure, thereby disrupting its planarity. This steric hindrance is postulated to influence the molecular packing, thereby determining the macroscopic pore geometry. Specifically, the enhanced planarity of the PyT-A may lead to tighter molecular packing, potentially reducing the specific surface area and pore volume. These BET result differences are well explained by their different molecular geometry in DFT calculation. This molecular geometry difference will not only influence their mixing behavior with CNTs but also further impact the overall thermoelectric performance of the nanohybrids. Further insights into the pore geometries of the two CMPs in different dispersion solvents are provided by the scanning electron microscope (SEM) images in Figure S13 (Supporting Information). There, the PyT-A exhibits a flake-like morphology indicative of stronger self-aggregation, whereas the PyT-T appears as spherical clusters. This further demonstrates the correlation between molecular structure and pore geometry.

2.2. Molecular Dynamics Simulation of CNT/CMP Nanohybrids

Molecular dynamics (MD) simulations were conducted using the Nanoscale Molecular Dynamics (NAMD) simulation package to examine the CMP wrapping behavior within a CNT/CMP nanohybrid system.[22] As depicted in **Figure 2**, the extent of CMPs coverage on the CNT surface is influenced by the structural disparities between the CMPs.[23] The center of mass (COM) positions of four CMP ligands relative to the center of the CNT serve as a metric for discerning the various interactions in the PyT-A and PyT-T,[24] as depicted in Figure 2a. Due to strong π–π interactions, both the PyT-A and PyT-T adhere to the CNT surface via their pyrene core structures. However, the wrapping behavior differs due to the different molecular geometries of the PyT-A and PyT-T. An examination of the PyT-A wrapped on the CNT reveals that the relative distances between the four ligands are comparable (Figure 2b), thereby indicating similar positions near the CNT surface. Additionally, the COM of the PyT-A is located at the pyrene core, thereby exhibiting the minimum distance from that of the CNT. This, in turn, suggests attachment to the CNT surface via the pyrene core. By contrast, while the PyT-T exhibits a similar distance between its COM and that of the CNT, the distances of the four ligands vary significantly (Figure 2c). This suggests less effective adhesion of the PyT-T to the CNT surface. Furthermore, half of the ligands in the PyT-T exhibit a greater distance from the CNT surface than those of the PyT-A.

The disparate wrapping phenomena of the PyT-A and PyT-T originate from their differing molecular geometries. The nonplanar thianthrene structure of PyT-T causes it to move away from the CNT surface, thereby resulting in a larger distance between the PyT-T and CNT. Although the MD simulation only estimates the monomeric structures of the two CMPs, it can be predicted that the differences in relative distance between the CNT and the two CMPs would be more pronounced when extended to the polymer form. Eventually, due to the imperfect wrapping

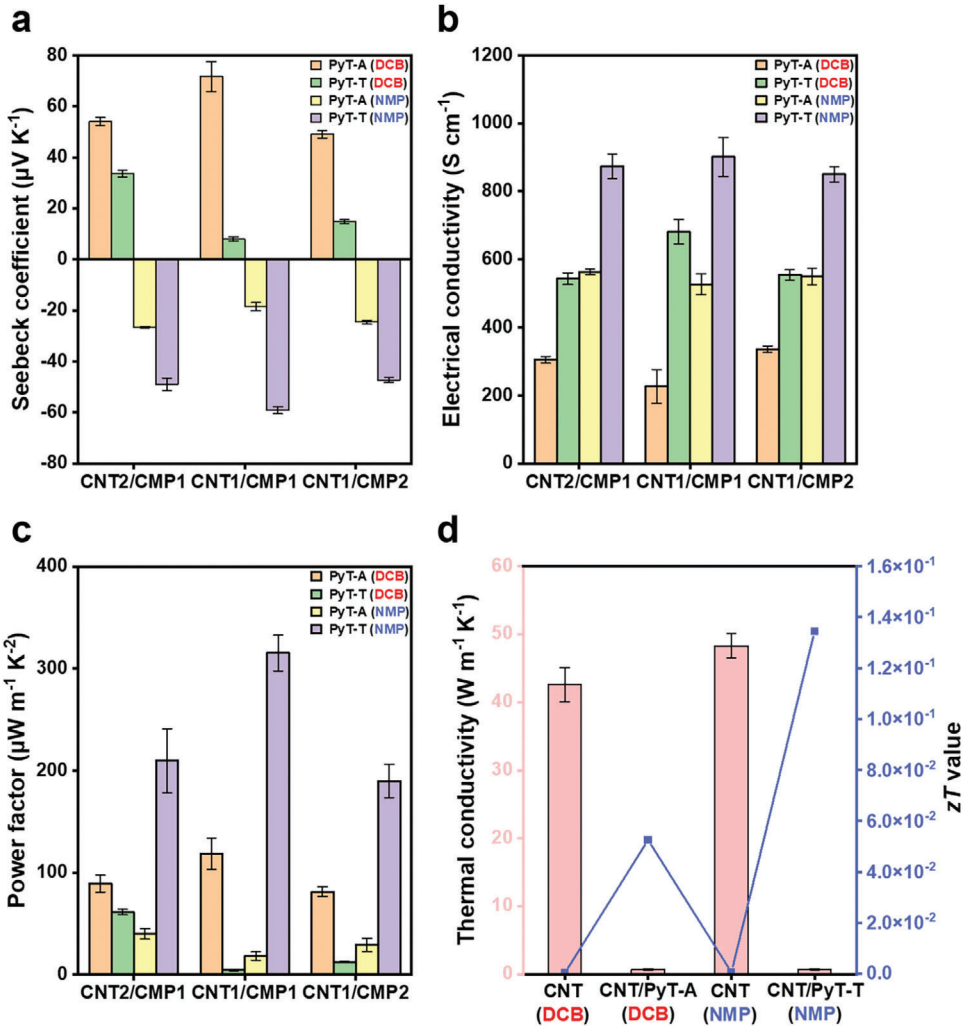

Figure 3. Thermoelectric performance assessment of CNT/CMP nanohybrids. a) Seebeck coefficient. b) Electrical conductivity. c) *PF* value. d) Thermal conductivity and resulting *zT* value.

behavior of the PyT-T, distinct interspaces emerge between the PyT-T and CNTs. Given the high environmental sensitivity of the CNT surface, these interspaces may have additional impacts on the thermoelectric properties of the nanohybrid system

2.3. Thermoelectric Performance of CNT/CMP Nanohybrids

The thermoelectric characteristics of the pristine CNT sample and the CNT/CMP nanohybrids are presented in **Figure 3**, Figure S14, and Table S1 (Supporting Information). As detailed in the Experimental Section, DCB was used as a p-type solvent, and NMP was used as an n-type solvent, in order to fabricate the p- and n-type nanohybrids. As shown in Figure 3a and Figure S14a (Supporting Information), the introduction of CMP has a significant influence on the Seebeck coefficient, with all of the CNT/PyT-A nanohybrids exhibiting a higher p-type Seebeck coefficient compared to the pristine CNT sample within the DCB dispersion group (28.41 μV K^{-1}). Moreover, the CNT1/PyT-A1 nanohybrid exhibits a noteworthy Seebeck coefficient of 71.7 μV K^{-1}, which can be attributed to the mitigation of the over-doping phenomenon facilitated by oxygen molecules. Specifically, the superior planar structure of the PyT-A may facilitate a more intimate attachment to the CNT surface, thereby shielding it from attack by oxygen molecules, thus leading to a higher Seebeck coefficient and a slightly diminished electrical conductivity (226.55 S cm^{-1}) compared to pristine CNT (539.42 S cm^{-1}) due to a reduced degree of p-type doping (Figure 3b). For both higher and lower weight ratios of PyT-A, the Seebeck coefficient is seen to decrease, while the electrical conductivity increases. This reduction can be attributed to two distinct reasons for CNT2/PyT-A1 and CNT1/PyT-A2 nanohybrids. Firstly, in the case of CNT2/PyT-A1 nanohybrid, the insufficient content of CMPs fails to adequately protect all CNT surfaces, leaving some areas vulnerable to oxygen attack. Conversely, for the CNT1/PyT-A2 nanohybrid, an excess amount of CMPs leads to self-aggregation, rendering some CMPs ineffective in guarding the CNT surfaces. Consequently, both these results in a relatively strong p-type doping effect compared to the CNT1/PyT-A1 nanohybrid. Conversely, the less planar structure of the PyT-T potentially exposes several interspaces to oxygen molecules, so the Seebeck coefficient of the CNT/PyT-T nanohybrid is

expected to be marginally lower than that of a pure CNT sample. In fact, the Seebeck coefficient of the CNT1/PyT-T1 nanohybrid is found to be 8.02 μV K^{-1}. This is because the PyT-T improves the CNT dispersion, thereby creating a denser CNT network by decreasing the CNT bundle size. This, in turn, increases the exposure area of oxygen molecules on the CNT surface, thus resulting in a more severe oxygen p-type doping impact. Indeed, a similar scenario occurs in the CNT/PyT-A; however, the PyT-A can adhere securely to the CNT surface, thereby preventing oxygen exposure. Simultaneously, the stronger p-type doping effect of the CNT/PyT-T nanohybrid is expected to enhance its electrical conductivity. Consequently, all of the CNT/PyT-T nanohybrids exhibit better electrical conductivity than either the pristine CNT sample or the CNT/PyT-A nanohybrids (Figure 3b; Figure S14b, Supporting Information). Thus, the CNT1/PyT-T1 nanohybrid dispersed in DCB achieves the greatest electrical conductivity of 681.20 S cm^{-1} owing to its strong p-type doping effect. Combining the findings of the Seebeck coefficient and electrical conductivity, these results indicate that the CNT1/PyT-A1 nanohybrid has a maximum power factor (*PF*) of 118.5 μW m^{-1} K^{-2} due to its high Seebeck coefficient.

In the case of the n-type solvent (NMP) group (Figure 3a and Figure S14a, Supporting Information), the opposite trend is observed due to the opposing n-type doping effect induced by the NMP solvent. Notably, the CNT/PyT-T nanohybrids exhibit higher Seebeck coefficients than both the pristine CNTs (−42.30 μV K^{-1}) and the CNT/PyT-A nanohybrids. In CNT/PyT-T nanohybrids, the superior thermoelectric performance compared to CNT/PyT-A nanohybrids can be attributed to a stronger n-type doping effect. The addition of CMPs into CNTs aids in their dispersion, promoting debundling and the formation of a denser CNT network, thereby increasing the exposed surface area to the outer environment. However, the crucial difference between PyT-T and PyT-A lies in their molecular geometry, particularly the steric hindrance effect. This difference will influence their wrapping behavior, as observed in the results of MD simulation (Figure 2). While both PyT-T and PyT-A aid in dispersing CNTs in NMP solvent, the close wrapping behavior of PyT-A leaves little excess surface area exposed to NMP, resulting in a weaker n-type doping effect. In contrast, PyT-T can create interspacing between itself and the CNT surface, allowing for increased exposure to NMP and consequently inducing a higher n-type doping effect. As a result, the CNT1/PyT-T1 nanohybrid dispersed in NMP exhibits a Seebeck coefficient of −59.1 μV K^{-1} and an electrical conductivity of 901.2 S cm^{-1} which is much higher than pristine CNT (594.99 S cm^{-1}), giving the highest *PF* of 315.3 μW m^{-1} K^{-2}. By contrast, the tight wrapping behavior of PyT-A impedes the CNT exposure to the NMP solvent, thus resulting in a poorer n-type doping effect and, hence, a lower Seebeck coefficient and electrical conductivity were achieved by the CNT/PyT-A nanohybrids. In summary, the molecular geometry difference of PyT-A and PyT-T will influence the wrapping behavior and further change the doping levels of nanohybrids. Furthermore, the molecular packing and self-aggregation phenomenon will also be influenced by their molecular geometry, resulting in different pore characteristics, which further affect their thermal transport property due to the different pore architecture. Subsequently, the thermal conductivity and zT values of the pristine CNTs and the CNT/CMP nanohybrids with the highest *PF* values are compared in Figure 3c. Here, the introduction of CMPs into the CNTs significantly reduces the thermal conductivity, thus resulting in a notable improvement in the zT value. Although direct measurement of the thermal conductivity of pristine CMPs still poses challenges in this work, theoretical evaluations can offer insights into the effects that CMP can decrease thermal conductivity. At first, thermal conductivity comprises two main contributions: electronic contribution (κ_e) and lattice contribution (κ_l). The former can be estimated using the Wiedemann–Franz law, which suggests that materials with high electrical conductivity typically exhibit high thermal conductivity. Conversely, materials with low electrical conductivity contribute minimally to overall thermal conductivity through the electronic pathway. Thus, for low electrical conductivity materials, thermal conductivity is primarily governed by κ_l. To reduce κ_l, strategies such as introducing porosity, grain boundaries, and interface barriers can impede phonon transport, thereby decreasing thermal conductivity. In the case of CMPs, their porous structure and amorphous nature severely hinder phonon transport, leading to significantly low thermal conductivity. Owing to the low thermal conductivity of CMPs, previous studies have utilized CMPs for thermal insulation applications,[12b,25] underscoring their potential for low thermal conductivity in this regard. Specifically, due to the low thermal conductivity and the suitable *PF* value, the maximum p- and n-type zT values are 0.053 and 0.13 for the CNT1/PyT-A1 in DCB and the CNT1/PyT-T1 in NMP. Although measuring the intrinsic thermoelectric properties of pristine CMPs poses challenges due to their high electrical resistance, the addition of CMPs to CNTs significantly impacts thermoelectric performance in the present work, influencing all thermoelectric parameters. Due to the distinct steric hindrance effect characterized by BET analysis and MD simulation, introducing CMPs allows for easy tuning of *PF* value with two different CMPs under different dispersion solvents. Furthermore, the pore structure in CMPs plays a significant role in decreasing the overall thermal conductivity of nanohybrids due to the more heterostructure interfaces and weaker molecular-molecular interaction; thereby enhancing the overall thermoelectric performance of CNT/CMP nanohybrids. Consequently, to achieve a comprehensive understanding of the relationship between the thermoelectric performance and the chemical structures of the two CMPs in these nanohybrids, the following analysis focuses on the doping phenomenon and interactions between the CNTs, CMPs, and solvents.

2.4. Photoluminescence Spectroscopy, Morphologies, and Microstructures of CNT/CMP Nanohybrids

The interactions between the CNTs and CMPs are elucidated by the solution-state photoluminescence (PL) spectra in Figure S15 (Supporting Information).[26] Here, both CMPs exhibit distinct PL peaks that are notably quenched upon the addition of CNTs. The PL quenching efficiency (PLQE) can be quantified by using the formula:

$$\mathrm{PLQE}\,(\%) = \left(I_0 - I/I_0\right) \times 100 \tag{2}$$

where I_0 is the pristine CMP peak intensity, and I is the corresponding peak intensity of the CNT/CMP nanohybrid.

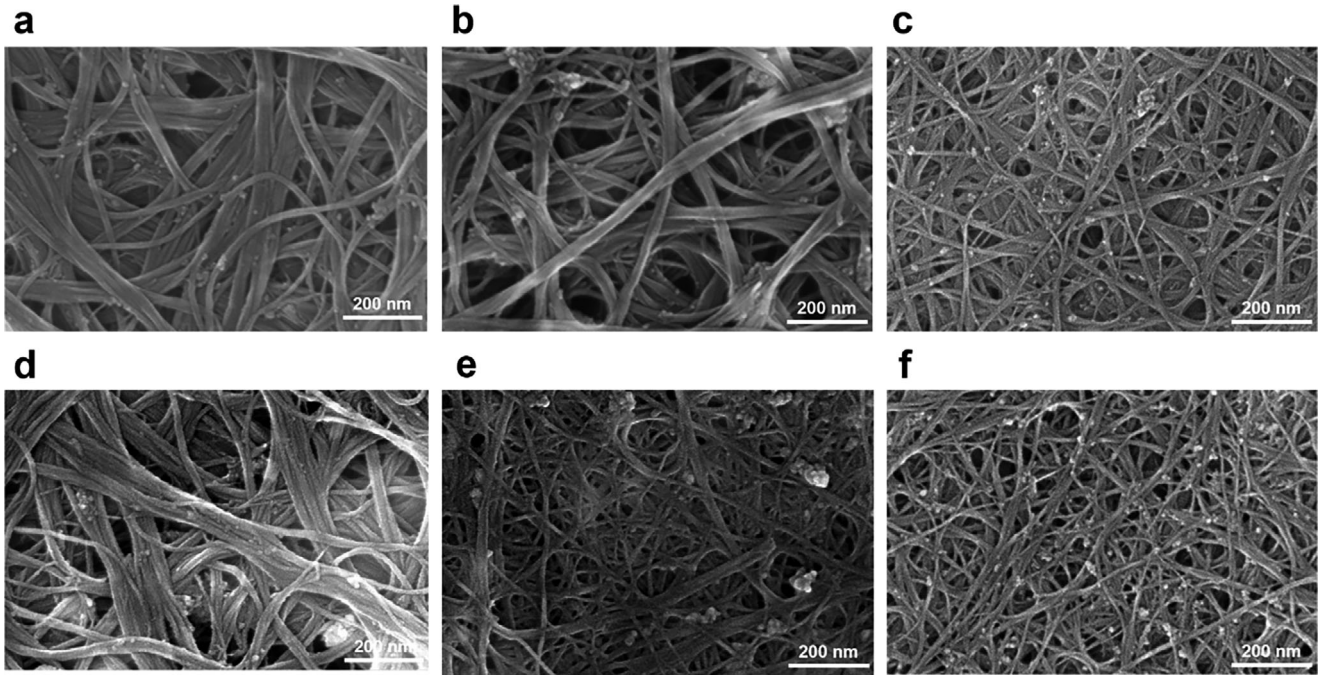

Figure 4. SEM images of CNT/CMP nanohybrids: a) CNT (DCB), b) CNT1/PyT-A1 (DCB), c) CNT1/PyT-T1 (DCB), d) CNT (NMP), e) CNT1/PyT-A1 (NMP), and f) CNT1/PyT-T1 (NMP). (scale bar = 200 nm).

Remarkably, both the CNT/PyT-A and CNT/PyT-T nanohybrids exhibit high PLQE values of over 90%, thereby indicating a pronounced wrapping of the CMPs around the CNTs.[27]

The surface morphologies of the various CNT/CMP nanohybrids are revealed by SEM, atomic force microscopy (AFM), and transmission electron microscopy (TEM) images in **Figures 4** and S16–S21 (Supporting Information). Notably, the morphologies of the nanohybrids that were prepared using the DCB and NMP solvents (Figure 4 and Figure S16, Supporting Information) each exhibit a noticeable reduction in bundle size relative to the pure CNT samples upon the addition of CMPs, thereby indicating effective enhancement of the CNT dispersion. Furthermore, the TEM images in Figure S17 (Supporting Information) reveal that the CNT/PyT-T nanohybrids have smaller bundle sizes of 20–30 nm compared to 20–40 nm for the CNT/PyT-A nanohybrids. Consistently with the SEM observations, the AFM images in Figures S18–S21 (Supporting Information) indicate that the addition of CMPs to the CNTs results in a more pronounced fiber-like morphology, along with a decrease in surface roughness due to the improved dispersion properties and reduced bundle aggregation. Moreover, in comparison to the PyT-A, the more non-planar structure of the PyT-T alleviates the strong self-aggregation phenomenon of the CMP, thereby resulting in a slightly smaller bundle size and smoother surface.

The microstructures of the CNT/CMP nanohybrids in the two different solvents are further revealed by the grazing incidence X-ray diffraction (GIXRD) in Figures S22 and S23 (Supporting Information). Here, the pristine CMPs reveal distinct powder ring signals in PyT-A under both DCB and NMP solvents, while no such signals are observed in the PyT-T patterns. This can be attributed to differences in the molecular structures of the PyT-A and PyT-T. Specifically, the pronounced self-aggregation tendency of the PyT-A (due to its substantial planarity) results in a relatively ordered molecular packing, which leads to multiple signals in PyT-A's GIXRD pattern. The introduction of CNT into the PyT-A nanohybrid disrupts the strong self-aggregation of PyT-A, resulting in the disappearance of PyT-A's characteristic ring signals. Instead, a broad CNT signal emerges. Conversely, for PyT-T, the steric hindrance effect prevents the observation of any distinct signals, and the difference after the introduction of CNT can only be discerned through the numerous CNT rings. Comparing the two nanohybrids, it becomes evident that the CNT signals in CNT/PyT-T are slightly more prominent than those in CNT/PyT-A. This difference may be attributed to the superior dispersion capability of PyT-T compared to PyT-A, which may likely be due to the absence of a self-aggregation phenomenon in PyT-T. The better dispersed CNTs may have a more ordered arrangement. Therefore, leading to a prominent diffraction signal. Furthermore, a comparison between CNT/PyT-T in DCB and CNT/PyT-T in NMP reveals that the latter exhibits more pronounced signals. This observation is possibly attributed to NMP being a superior dispersion solvent compared to DCB.

2.5. Validation of the Doping Phenomenon in CNT/CMP Nanohybrids

In this section, the interspacing phenomena in the CNT/CMP nanohybrids under various conditions are investigated to determine the resulting impacts on their thermoelectric behaviors. First, the pristine Raman spectra of PyT-A and PyT-T are shown in Figure S24 (Supporting Information). Furthermore, the Raman spectra of the various CNT/CMP nanohybrids in **Figure 5** each exhibit two prominent peaks due to the CNTs, including

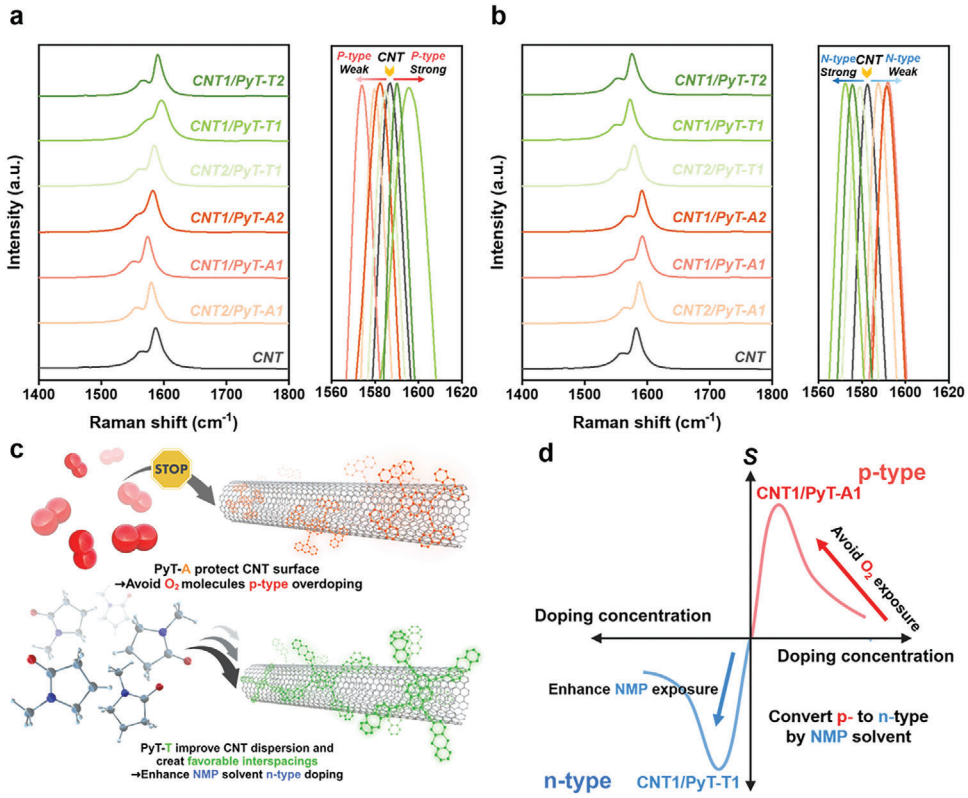

Figure 5. Raman spectra of CNT/CMP nanohybrid a) with DCB solvent and b) with NMP solvent. c) Schematic representation of interaction among CNT, CMP, and external environment. d) Correlation plot depicting the relationship between Seebeck coefficient and doping concentration (The left part of the curve belongs to the NMP solvent group, whereas the right region belongs to the DCB solvent group.).

the defect-originated D-band at ≈1350 cm^{-1} and the graphite-originated G-band ≈1590 cm^{-1}.[28] Combination the observation in Figure 5a,b (Raman spectra of the various CNT/CMP nanohybrids), it becomes apparent that upon the incorporation of CMPs into CNTs, alterations are observed solely in the position of the G-band, with no emergence of new peaks discernible. This phenomenon may be attributed to the absence of distinctive peaks formed by the interaction between CNTs and CMPs. Furthermore, the relatively low intensity of the Raman peaks of CMPs and their proximity to the 1500 cm^{-1} region further let them be covered by the strong CNT G-band peak. Consequently, within Figure 5a,b, there are no additional peaks corresponding to CMPs that can be notable. The doping level of the CNTs is revealed by the amount of displacement in the G-band.[29] Thus, in the DCB solvent group, the G-band of the CNT/PyT-A nanohybrid (Figure 5a) exhibits a red shift relative to the pristine CNTs, thereby indicating a relatively weak p-type doping effect, while that of the CNT/PyT-T nanohybrid exhibits a blue shift, signifying a stronger p-type doping effect (Figure 5b). In particular, the CNT1/PyT-A1 exhibits the strongest G-band redshift, thereby indicating the weakest p-type doping effect. Within the NMP solvent group, however, the CNT/PyT-A nanohybrids exhibit a blue shift relative to the pure CNTs, thereby indicating weak n-type doping due to the NMP solvent, while the CNT1/PyT-T1 nanohybrids exhibit an obvious red shift, thereby indicating a much stronger n-type doping effect. These results are consistent with the above discussion on the Seebeck coefficients.

Next, the work function (W_f) of each nanohybrid can be determined from the ultraviolet photoelectron spectra (UPS) in Figures S25 and S26 (Supporting Information), and the results are summarized in Table S2 (Supporting Information). Here, significant alterations in W_f are observed after introducing CMPs into the CNTs. In the case of the DCB solvent group (Figure S25, Supporting Information), the W_f of the CNT/PyT-A nanohybrid is decreased relative to that of the pristine CNTs, thereby indicating a reduction in the p-type doping effect after PyT-A addition.[30] Moreover, the W_f of CNT1/PyT-A1 nanohybrid will drop to the deepest value of 4.20 eV, thereby indicating the smallest p-type doping effect. Meanwhile, the CNT2/PyT-A1 and CNT1/PyT-A2 nanohybrids exhibit slightly higher W_f values due to a slightly stronger p-type doping effect. By contrast, the CNT1/PyT-T1 nanohybrids exhibit the highest W_f values due to the strongest p-type doping effects. In the NMP solvent group, however, the CNT1/PyT-T1 nanohybrid exhibits the substantially lowest W_f of 3.46 eV, thereby indicating a significant n-type doping effect from the NMP solvent (Figure S26, Supporting Information), while the CNT2/PyT-T1 and CNT1/PyT-T2 nanohybrids have slightly higher W_f values due to a lesser n-type doping effect. Nevertheless, the highest W_f and, hence, the lowest n-type doping impact, is observed for the CNT1/PyT-A1 nanohybrid, thereby indicating the combined effect of solvent and molecular geometry.

In addition, Hall effect measurements were used to determine the carrier concentration in each nanohybrid, and the results are

presented in Table S3 (Supporting Information). Thus, in the DCB solvent, all samples exhibit p-type characteristics, indicative of a hole transport mechanism. The carrier concentrations align with the doping levels indicated by the Raman G-band displacements and by the W_f values determined by UPS. The introduction of PyT-A into the CNTs results in a reduction in carrier concentration and electrical conductivity due to the weaker oxygen p-type doping effect. Conversely, the CNT/PyT-T nanohybrids exhibit higher carrier concentrations due to the stronger p-type doping effect. In the NMP solvent, however, all samples exhibit n-type carrier characteristics, thereby denoting an electron transport mechanism. Moreover, the CNT/PyT-T nanohybrids exhibit higher carrier concentrations due to the stronger n-type doping effect, while the CNT/PyT-A nanohybrids exhibit lower carrier concentrations.

In conclusion, by integrating the results of Raman spectroscopy, UPS, and Hall effect measurements, the various doping levels and charge-carrier types of the CNT/CMP nanohybrids are confirmed. Moreover, the reasons for these various characteristics are explained by DFT computation and MD simulation. Owing to the difference in molecular geometry between the PyT-A and PyT-T, along with the different CMP weight ratios, the shielding behavior can be modulated to expose the CNT surface to the external environment to varying degrees, as illustrated in Figure 5c. As a result, the Seebeck coefficient changes as the doping concentration of the nanohybrid varies. For the p-type nanohybrids, the trend in the Seebeck coefficient is revealed by the right-hand region of the curve in Figure 5d.[31] Here, because CNTs are normally overdoped with oxygen molecules under atmospheric conditions, the shielding of the PyT-A can minimize the doping concentration and therefore achieve the greatest Seebeck coefficient. By contrast, in the case of the n-type nanohybrids (left-hand region, Figure 5d), the n-type property is derived from the NMP solvent. Consequently, the more open structure caused by the larger distance between the non-planar PyT-T and CNT can act to boost the NMP doping effect to convert the CNTs from p-type to n-type.[32] In other words, the introduction of PyT-T can enhance the exposure of the CNT surface to the NMP, thus resulting in a higher n-type Seebeck coefficient.

2.6. Stability Test and Performance Comparison of CNT/CMP Nanohybrids

The long-term storage stabilities of the various CNT/CMP nanohybrids are compared with that of the pristine CNT in Figure S27a,b (Supporting Information) for the DCB and NMP groups, respectively. Here, the CNT1/PyT-A1 dispersed in DCB and the CNT1/PyT-T1 dispersed in NMP each exhibit notable stability compared to the pristine CNT samples. This can be attributed to the effective protection of the CNTs by the CMPs. In the case of the CNT1/PyT-A1 in DCB, the tight wrapping of the CNTs by the PyT-A serves as a barrier against oxygen molecules from the surrounding environment, while the looser wrapping of the CNTs by the PyT-T in NMP facilitates exposure of the CNT surface to more NMP molecules while still protecting the surface from the external environment.

The thermoelectric performances of the optimized CNT1/PyT-A1 (DMB) and CNT1/PyT-T1 (NMP) nanohybrids are compared with those of previously reported porous materials (e.g., MOF-based thermoelectrics) in **Figure 6** and S4 (Supporting Information).[33] Here, the distinctive fully-conjugated porous structures of the CNT/CMP nanohybrids lead to acceptable *PF* values and low thermal conductivity, thereby providing superior zT values.

2.7. Demonstration of a Prototype CNT/CMP Thermoelectric Generator

A prototype thermoelectric generator (TEG) was constructed using six pairs of p-n junctions connected in series, as detailed in the Experimental section. The p- and n-type legs were fabricated from the CNT1/PyT-A1 (DCB) and CNT1/PyT-T1 (NMP) nanohybrids, which were chosen for their greatest zT values. The layout of the TEG was designed as a flexible lateral-type device, suitable for wearable thermoelectric applications, as shown in **Figure 7a**. The TEG was easily affixed to a polyethylene terephthalate (PET) substrate, as depicted in Figure 7c. The theoretical output voltage (V_{oc}) values of the device at temperature differences (ΔT) of 5, 10, 15, and 20 K are determined by taking the Seebeck coefficients of the p-type leg (71.7 μV K^{-1}) and n-type leg (−59.1 μV K^{-1}) and multiplying by the number of leg pairs and the specific temperature difference. For example, at a ΔT of 20 K, the ideal V_{oc} is calculated to be (71.7 + 59.1) μV K^{-1} × 6 × 20 K = 15.7 mV. As shown in Figure 7b, the measured V_{oc} values (with the heat sink set at 298 K) are 3.4, 7.5, 11.4, and 15.6 mV, respectively, which are closely aligned with theoretical V_{oc} values. This can be attributed to the low thermal conductivities of the CNT/CMP nanohybrids, which facilitate the maintenance of the applied ΔT across the TEG. Consequently, the actual ΔT closely approximates that between the heat source and heat sink. Combining these findings with the measured currents, the maximum power (P_{max}) values at ΔT = 5, 10, 15, and 20 K are found to be 10.1, 50.6, 106.6, and 196.6 nW, respectively.

In addition, the bending properties of the TEG are thoroughly demonstrated in Figure 7c,d, and Figure S28 (Supporting Information). Here, the TEG's internal resistance and V_{oc} are well maintained under bending ratios of 0% (full length = 14 cm), 30% (10 cm), 50% (7 cm), and 80% (3 cm). Additionally, a cyclic bending test conducted at the highest bending ratio (80%) demonstrates minimal deterioration in internal resistance and V_{oc} after a thousand bending cycles (Figure S28c, Supporting Information), thereby indicating remarkable adaptability for wearable applications. Furthermore, the environmental stability of the TEG is demonstrated in Figure S28d (Supporting Information), where the output performance remains stable after one month of storage under ambient conditions.

3. Conclusions

In summary, this work elucidates the pioneering use of conjugated microporous polymer (CMP)-based materials in thermoelectric applications. Specifically, highly-conducting carbon nanotubes (CNTs) were dispersed in 1,2-dichlorobenzene (DCB) or N-methyl-2-pyrrolidone (NMP)) to fabricate respective p- and n-type CNT/CMP nanohybrids. Furthermore, through a meticulous chemical structure design strategy, the molecular geometry

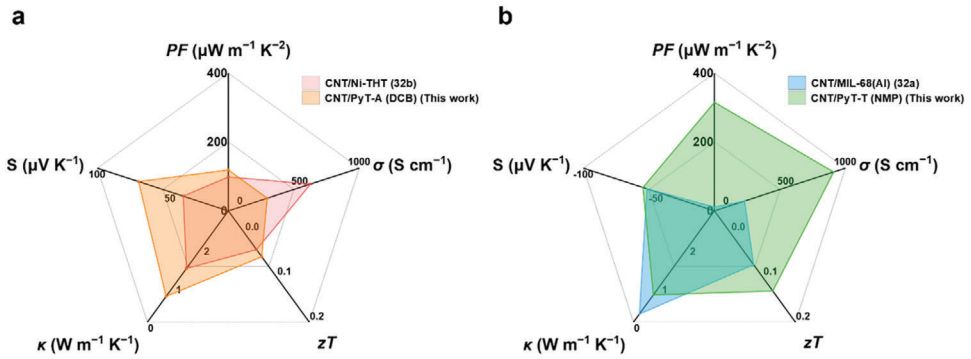

Figure 6. Comparative analysis of thermoelectric performance between the current study and previous investigations focused on porous-based thermoelectric materials: Evaluation of a) P-type and b) N-type thermoelectric studies.

and the pore structures were altered to achieve an enhanced thermoelectric performance. As well as manipulating the choice of dispersion solvent, the doping level was modulated via distinct steric hindrance effects of CMPs with different ligands (namely, thianthrene (T) or anthracene (A)) on the pyrene (Py) core, giving optimal p- and n-type zT values of 0.053 and 0.13 for the CNT/PyT-A nanohybrid in DCB and the CNT/PyT-T nanohybrid in NMP, respectively. Additionally, a flexible thermoelectric generator with six pairs of the as-fabricated p-n junctions in series presented an open-circuit voltage (V_{oc}) of 15.6 mV and maximum power (P_{max}) of 196.6 nW. The present study not only diversifies the application scope of innovative CMP-based materials but also

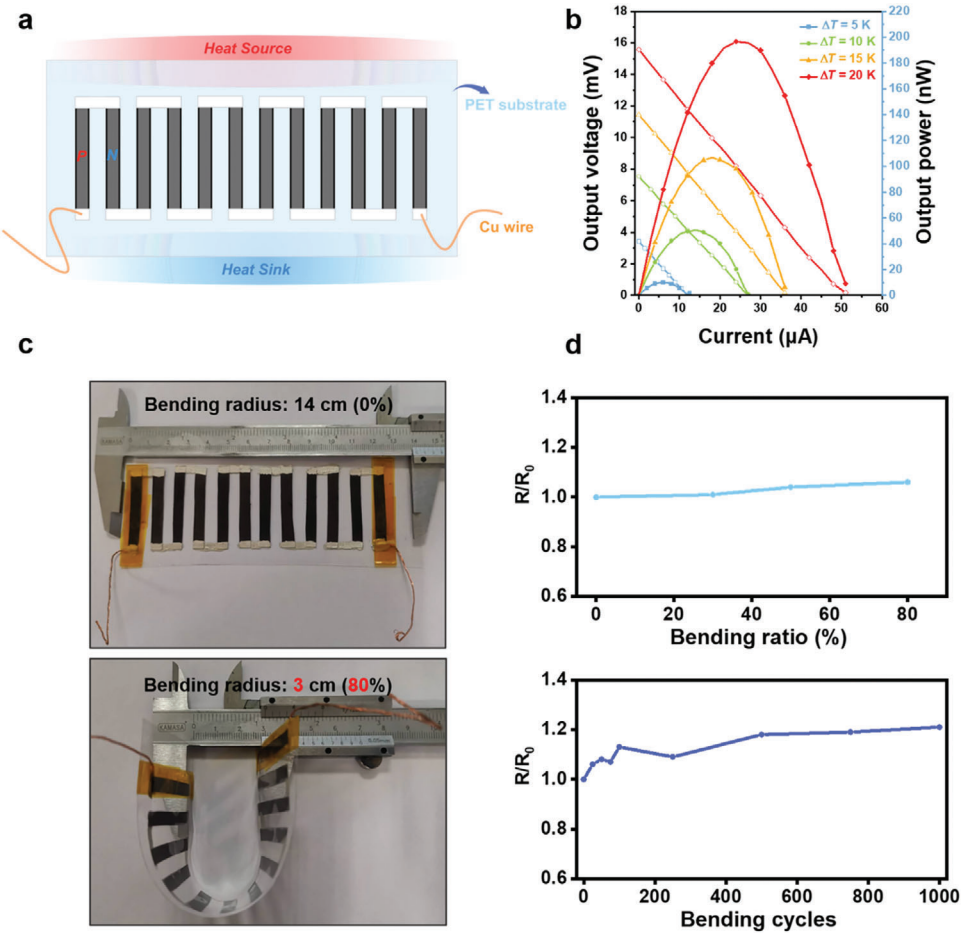

Figure 7. Illustration of a prototype CNT/CMP-based TEG: a) Schematic representation of CNT/CMP-based TEG. b) Output characteristics of the TEG consisting of 6 pairs of legs under different temperature differences. c) Photographic images of the TEG under the flat condition and bending test. d) Analysis of the internal resistance under different bending ratios and cycles.

exhibits a high-performance thermoelectric nanohybrid, thereby contributing significantly to the advancement of thermoelectric research.

4. Experimental Section

Synthesis of PyT-A and PyT-T CMPs: For the synthesis of the PyT-A CMP, Py-T (5 g, 16.6 mmol), An—Br_2 (11.2 g, 33.2 mmol), $Pd(PPh_3)_4$ (1.93 g, 1.66 mmol), CuI (2 g, 10.4 mmol), and PPh_3 (2 g, 7.6 mmol) were added to a 1:1 mixture of Et_3N and DMF in a flame-dried Schlenk tube, and the mixture was refluxed at 90 °C for 3 days under an atmosphere of nitrogen (N_2).[34] The resulting black precipitate was filtered and purified by using Soxhlet extraction in THF. To synthesize the PyT-T CMP, Py-T (5 g, 16.6 mmol), Th—Br_2 (12.33 g, 33 mmol), $Pd(PPh_3)_4$ (1.93 g, 1.66 mmol), CuI (2 g, 10.4 mmol), and PPh_3 (2 g, 7.6 mmol) were introduced to a 1:1 mixture of Et_3N/DMF in a flame-dried Schlenk tube, and the mixture was similarly refluxed at 90 °C for 3 days under an N_2 atmosphere. The solid was then dried at 60 °C overnight to afford PyT-T CMP as a dark red powder.[21]

Preparation of CNT/CMP Nanohybrid Solution: For this procedure, the as-synthesized PyT-A and PyT-T CMPs powders were pre-heated in a vacuum oven at 100 °C for 12 h to eliminate any adsorbed solvent or gas molecules. In the solution preparation process, a fixed weight of 2 mg for the CNT component was added to each nanohybrid. To achieve different nanohybrid compositions, the amount of CMP was adjusted accordingly. For instance, in the case of CNT2/CMP1, the weight of CMP was set at 1 mg, resulting in a CMP weight ratio of ≈33%. Similarly, for CNT1/CMP1, the weight of CMP was 2 mg (CMP% = 50%), and for CNT1/CMP2, the weight of CMP was 4 mg (CMP% = 67%). Additionally, a total solid concentration of 1 mg mL^{-1} throughout the experiment was maintained. Then, solutions of the different amounts of PyT-A and PyT-T powders in both DCB and NMP solvents were prepared. Each solution was stirred at 100 °C for 3 h to ensure complete dissolution. Next, 2 mg of CNTs were added to each solution and thoroughly mixed using a ball mill (Restch MM440) at 30 Hz for 15 min. In addition, a pure CNT solution was prepared by a similar procedure, but without adding the CMP powder.

Fabrication and Measurement of Nanohybrid Thermoelectric Film: First, the glass substrates (7.5 × 15 mm^2) would be cleaned with acetone, isopropanol, and deionized water in an ultrasonic bath. After that, the glass substrates were subjected to additional cleaning by O_3 plasma cleaning treatment. Next, the glass substrates were pre-heated on a hot plate for the following drop-casting process with DCB solvent applied at 100 °C and NMP solvent applied at 150 °C. After the pre-heating stage, a 30 µL of nanohybrid solution was drop-casted onto the pre-heated substrates three times. The wet film was subjected to a drying process under the heating conditions. The thicknesses of the resulting nanohybrid films were ≈10 µm. Before measuring the thermoelectric properties, the nanohybrid thin films were subjected to an annealing process at 190 °C for 15 min to promote better interfacial contact between the CNTs and the CMPs. All the thin film casting and heating procedures were conducted in an N_2-filled glove box. The thermoelectric properties of the nanohybrid films, including the Seebeck coefficient and electrical conductivity, were evaluated using commercial thermoelectric performance test equipment (ZEM-3, ADVANCE RIKO Inc., Japan) at a temperature of 303 K under a helium atmosphere. The experiments will include three different temperature differences between the hot and cold sides of the samples. By systematically varying these temperature gradients, a regression line of Seebeck coefficient can be obtained. The silver paste was applied to both ends of the device for better electrical conductance during thermoelectric measurement. The thermal conductivities of the pristine CNT film and the nanohybrid films were measured using a Hot Disk TPS 2500S thermal constant analyzer equipped with a thin film module via the transient plane source (TPS) method at a constant temperature of 25 °C controlled by an air conditioner. To meet the criteria of the thin film measurement module, the pristine CNT film and the nanohybrid films would be fabricated by vacuum infiltration method to get thicker and larger samples. The test method for low thermal conductivity thin films was according to the previously reported procedure.[35]

Fabrication and Measurement of the Thermoelectric Generator: The nanohybrid films with the highest *zT* values were selected for fabricating the thermoelectric generator device. Specifically, the CNT1/PyT-A1 (DCB) and CNT1/PyT-T1 (NMP) were selected for the p- and n-type legs, respectively. The thermoelectric legs were fabricated by drop-casting the solution on a polyimide substrate. The casting condition is identical to the preceding phase. The films were then sliced into rectangular shapes with a width of 7 mm, a length of 30 mm, and a thickness of 10 µm. Each thermoelectric leg was then affixed to a flexible polyethylene terephthalate (PET) substrate using a double-sided tape. Consecutive p-n junctions were established by employing conducting silver paint, resulting in a total of 6 junctions in series. Finally, copper wires were employed to establish connections to an external circuit, ensuring optimal electrical contact. The performance of the thermoelectric generator was measured using a custom-built system under an ambient environment. The temperature gradient was controlled by water-cooling systems at both the heat source and the heat sink. The temperature of the heat sink was fixed at 298 K, and various temperature gradients were realized by adjusting the temperature of the heat source. The K-type thermocouple was attached to the thermoelectric generator surface to monitor the real device temperature using a Keithley DAQ 6510 multimeter system. The output voltage and short-circuit current were measured by connecting the Cu wires with Cu probes and collected using a Keithley 2182A nanovoltmeter and Keithley 2400 sourcemeter, respectively.

Statistical Analysis: Descriptive statistics were used to derive the mean and standard deviation in the analysis of quintuplicate measurements of electrical conductivity, thermal conductivity, and Seebeck coefficient. All computations were performed using the OriginLab software.

Supporting Information

Supporting Information is available from the Wiley Online Library or from the author.

Acknowledgements

M.H.L. and M.G.M. contributed equally to this work. This work was supported by 2030 Cross-Generation Young Scholars Program by the National Science and Technology Council (NSTC) in Taiwan under grant 113-2628-E-002-009 and under grant 112-2124-M-002-013, Academic Research-Career Development Project (Sprout Research Projects) by National Taiwan University (NTU113L7839), and Advanced Research Center for Green Materials Science and Technology from The Featured Area Research Center Program within the framework of the Higher Education Sprout Project by the Ministry of Education (112L9006). S. W.K. also acknowledges the financial support from NSTC under grants 110-2124-M-002-013 and 111-2223-E-110-004.

Conflict of Interest

The authors declare that they have no conflict of interest.

Data Availability Statement

The data that support the findings of this study are available from the corresponding author upon reasonable request.

Keywords

carbon nanotube, conjugated microporous polymers, high *zT*, nanohybrids, thermoelectric

Received: April 11, 2024
Revised: May 19, 2024
Published online: May 27, 2024

[1] a) J. He, T. M. Tritt, *Science* **2017**, *357*, eaak9997; b) L. Deng, Y. Liu, Y. Zhang, S. Wang, P. Gao, *Adv. Funct. Mater.* **2023**, *33*, 2210770; c) M. Massetti, F. Jiao, A. J. Ferguson, D. Zhao, K. Wijeratne, A. Würger, J. L. Blackburn, X. Crispin, S. Fabiano, *Chem. Rev.* **2021**, *121*, 12465.
[2] C. Gayner, K. K. Kar, *Prog. Mater Sci.* **2016**, *83*, 330.
[3] a) G. Tan, L. D. Zhao, M. G. Kanatzidis, *Chem. Rev.* **2016**, *116*, 12123; b) C. Chang, M. Wu, D. He, Y. Pei, C. F. Wu, X. Wu, H. Yu, F. Zhu, K. Wang, Y. Chen, L. Huang, J. F. Li, J. He, L. D. Zhao, *Science* **2018**, *360*, 778; c) C. Xiao, Z. Li, K. Li, P. Huang, Y. Xie, *Acc. Chem. Res.* **2014**, *47*, 1287.
[4] a) B. T. McGrail, A. Sehirlioglu, E. Pentzer, *Angew. Chem., Int. Ed.* **2015**, *54*, 1710; b) K. Yusupov, A. Vomiero, *Adv. Funct. Mater.* **2020**, *30*, 2002015; c) J. Liang, R. Cui, X. Zhang, K. Koumoto, C. Wan, *Adv. Funct. Mater.* **2023**, *33*, 2208813; d) N. Nandihalli, C. J. Liu, T. Mori, *Nano Energy* **2020**, *78*, 105186; e) Y. Xue, C. Gao, L. Liang, X. Wang, G. Chen, *J. Mater. Chem. A* **2018**, *6*, 22381; f) J. Tang, Y. Chen, S. R. McCuskey, L. Chen, G. C. Bazan, Z. Liang, *Adv. Electron. Mater.* **2019**, *5*, 1800943.
[5] a) M. H. Lee, Y. H. Kang, J. Kim, Y. K. Lee, S. Y. Cho, *Adv. Energy Mater.* **2019**, *9*, 1900914; b) J. Li, Q. Shi, J. A. Röhr, H. Wu, B. Wu, Y. Guo, Q. Zhang, C. Hou, Y. Li, H. Wang, *Adv. Funct. Mater.* **2020**, *30*, 2002508; c) Y. Fan, Z. Liu, G. Chen, *Small* **2021**, *17*, 2100505; d) A. J. Ahmed, M. S. A. Hossain, S. M. Kazi Nazrul Islam, F. Yun, G. Yang, R. Hossain, A. Khan, J. Na, M. Eguchi, Y. Yamauchi, X. Wang, *ACS Appl. Mater. Interfaces* **2020**, *12*, 28057; e) J. F. Olorunyomi, B. P. Dyett, B. J. Murdoch, A. J. Ahmed, G. Rosengarten, R. A. Caruso, C. M. Doherty, X. Mulet, *Adv. Funct. Mater.* **2024**, 2403644.
[6] S. Das, P. Heasman, T. Ben, S. Qiu, *Chem. Rev.* **2017**, *117*, 1515.
[7] L. Tan, B. Tan, *Chem. Soc. Rev.* **2017**, *46*, 3322.
[8] K. Geng, T. He, R. Liu, S. Dalapati, K. T. Tan, Z. Li, S. Tao, Y. Gong, Q. Jiang, D. Jiang, *Chem. Rev.* **2020**, *120*, 8814.
[9] J. S. M. Lee, A. I. Cooper, *Chem. Rev.* **2020**, *120*, 2171.
[10] a) A. Molina, N. Patil, E. Ventosa, M. Liras, J. Palma, R. Marcilla, *ACS Energy Lett.* **2020**, *5*, 2945; b) W. Wu, Z. Li, S. Liu, D. Zhang, B. Cai, Y. Liang, M. Wu, Y. Liao, X. Zhao, *Angew. Chem., Int. Ed.* **2024**, *63*, e202404563.
[11] J. Kim, J. H. Kim, K. Ariga, *Joule* **2017**, *1*, 739.
[12] a) N. Chaoui, M. Trunk, R. Dawson, J. Schmidt, A. Thomas, *Chem. Soc. Rev.* **2017**, *46*, 3302; b) W. Zhang, H. Zuo, Z. Cheng, Y. Shi, Z. Guo, N. Meng, A. Thomas, Y. Liao, *Adv. Mater.* **2022**, *34*, 2104952.
[13] a) W. Lyu, W. Zhang, H. Liu, Y. Liu, H. Zuo, C. Yan, C. F. J. Faul, A. Thomas, M. Zhu, Y. Liao, *Chem. Mater.* **2020**, *32*, 8276; b) Z. Zhou, D. Guo, D. B. Shinde, L. Cao, Z. Li, X. Li, D. Lu, Z. Lai, *ACS Nano* **2021**, *15*, 11970; c) K. Yusupov, S. Stumpf, S. You, A. Bogach, P. M. Martinez, A. Zakhidov, U. S. Schubert, V. Khovaylo, A. Vomiero, *Adv. Funct. Mater.* **2018**, *28*, 1801246; d) X. Sun, Y. Wang, K. Li, J. Wang, X. Dai, D. Chong, J. Yan, H. Wang, *Adv. Funct. Mater.* **2022**, *32*, 2203080.
[14] a) A. D. Avery, B. H. Zhou, J. Lee, E. S. Lee, E. M. Miller, R. Ihly, D. Wesenberg, K. S. Mistry, S. L. Guillot, B. L. Zink, Y. H. Kim, J. L. Blackburn, A. J. Ferguson, *Nat. Energy* **2016**, *1*, 16033; b) W. Deng, L. Deng, Z. Li, Y. Zhang, G. Chen, *ACS Appl. Mater. Interfaces* **2021**, *13*, 12131.
[15] Y. Zhang, Q. Zhang, G. Chen, *Carbon Energy* **2020**, *2*, 408.
[16] a) B. A. MacLeod, N. J. Stanton, I. E. Gould, D. Wesenberg, R. Ihly, Z. R. Owczarczyk, K. E. Hurst, C. S. Fewox, C. N. Folmar, K. Holman Hughes, B. L. Zink, J. L. Blackburn, A. J. Ferguson, *Energy Environ. Sci.* **2017**, *10*, 2168; b) J. Y. Kim, W. Lee, Y. H. Kang, S. Y. Cho, K. S. Jang, *Carbon* **2018**, *133*, 293; c) J. Tang, R. Chen, L. Chen, G. C. Bazan, Z. Liang, *J. Mater. Chem. A* **2020**, *8*, 9797.
[17] a) M. M. Samy, M. G. Mohamed, A. F. M. El-Mahdy, T. H. Mansoure, K. C. W. Wu, S. W. Kuo, *ACS Appl. Mater. Interfaces* **2021**, *13*, 51906; b) A. Molina, N. Patil, E. Ventosa, M. Liras, J. Palma, R. Marcilla, *Adv. Funct. Mater.* **2020**, *30*, 1908074; c) W. Lyu, C. Yan, Z. Chen, J. Chen, H. Zuo, L. Teng, H. Liu, L. Wang, Y. Liao, *ACS Appl. Energy Mater.* **2022**, *5*, 3706.
[18] a) H. Wang, C. Yu, *Joule* **2019**, *3*, 53; b) N. Pataki, P. Rossi, M. Caironi, *Appl. Phys. Lett.* **2022**, 121; c) Y. Wang, L. Yang, X. L. Shi, X. Shi, L. Chen, M. S. Dargusch, J. Zou, Z. G. Chen, *Adv. Mater.* **2019**, *31*, 1807916.
[19] W. Zhou, Q. Fan, Q. Zhang, L. Cai, K. Li, X. Gu, F. Yang, N. Zhang, Y. Wang, H. Liu, W. Zhou, S. Xie, *Nat. Commun.* **2017**, *8*, 14886.
[20] a) Y. Wang, Q. Li, J. Wang, Z. Li, K. Li, X. Dai, J. Pan, H. Wang, *Nano Energy* **2022**, *93*, 106804; b) S. Hata, M. Shiraishi, S. Yasuda, G. Juhasz, Y. Du, Y. Shiraishi, N. Toshima, *Energy Mater. Adv.* **2022**, *2022*.
[21] M. G. Mohamed, S. V. Chaganti, M. S. Li, M. M. Samy, S. U. Sharma, J. T. Lee, M. H. Elsayed, H. H. Chou, S. W. Kuo, *ACS Appl. Energy Mater.* **2022**, *5*, 6442.
[22] W. Gomulya, G. D. Costanzo, E. J. F. de Carvalho, S. Z. Bisri, V. Derenskyi, M. Fritsch, N. Fröhlich, S. Allard, P. Gordiichuk, A. Herrmann, S. J. Marrink, M. C. dos Santos, U. Scherf, M. A. Loi, *Adv. Mater.* **2013**, *25*, 2948.
[23] S. S. Tallury, M. A. Pasquinelli, *J. Phys. Chem. B.* **2010**, *114*, 4122.
[24] B. Yu, S. Fu, Z. Wu, H. Bai, N. Ning, Q. Fu, *Compos. – A: Appl. Sci. Manuf.* **2015**, *73*, 155.
[25] H. Wei, F. Wang, H. Sun, Z. Zhu, C. Xiao, W. Liang, B. Yang, L. Chen, A. Li, *J. Mater. Chem. A* **2018**, *6*, 8633.
[26] P. Rohringer, L. Shi, X. Liu, K. Yanagi, T. Pichler, *Carbon* **2014**, *74*, 282.
[27] P. S. Lin, S. Inagaki, J. H. Liu, M. C. Chen, T. Higashihara, C. L. Liu, *Chem. Eng. J.* **2023**, *458*, 141366.
[28] Z. Li, L. Deng, I. A. Kinloch, R. J. Young, *Prog. Mater Sci.* **2023**, *135*, 101089.
[29] a) M. S. Dresselhaus, P. C. Eklund, *Adv. Phys.* **2000**, *49*, 705; b) Q. H. Yang, P. X. Hou, M. Unno, S. Yamauchi, R. Saito, T. Kyotani, *Nano Lett.* **2005**, *5*, 2465.
[30] S. Horike, Q. Wei, K. Akaike, K. Kirihara, M. Mukaida, Y. Koshiba, K. Ishida, *Nat. Commun.* **2022**, *13*, 3517.
[31] A. V. da Rosa, J. C. Ordóñez, in *Fundamentals of Renewable Energy Processes*, 4th Ed., (Eds: A. V. da Rosa, J. C. Ordóñez), Academic Press, Oxford **2022**, 187.
[32] P. S. Lin, J. M. Lin, S. H. Tung, T. Higashihara, C. L. Liu, *Small* **2024**, *20*, 2306166.
[33] a) M. H. Lin, C. H. Hsu, D. Y. Kang, C. L. Liu, *Chem. Eng. J.* **2024**, *485*, 149732; b) Z. Chen, Y. Cui, L. Liang, H. Wang, W. Xu, Q. Zhang, G. Chen, *Mater. Today Nano* **2022**, *20*, 100276; c) Y. H. Kang, E. J. Bae, M. H. Lee, M. Han, B. J. Kim, S. Y. Cho, *Small* **2022**, *18*, 2270020; d) X. Wang, L. Liang, H. Lv, Y. Zhang, G. Chen, *Nano Energy* **2021**, *90*, 106577; e) J. Li, B. Xia, X. Xiao, Z. Huang, J. Yin, Y. Jiang, S. Wang, H. Gao, Q. Shi, Y. Xie, J. Chen, *ACS Nano* **2023**, *17*, 19232; f) S. Liu, M. Lan, G. Li, Y. Piao, H. Ahmoum, Q. Wang, *Energy* **2021**, *225*, 120320.
[34] a) P. N. Singh, M. G. Mohamed, S. W. Kuo, *ACS Appl. Energy Mater.* **2023**, *6*, 11342; b) M. G. Mohamed, S. V. Chaganti, S. U. Sharma, M. M. Samy, M. Ejaz, J. T. Lee, K. Zhang, S. W. Kuo, *ACS Appl. Energy Mater.* **2022**, *5*, 10130.
[35] X. Liao, J. Denk, T. Tran, N. Miyajima, L. Benker, S. Rosenfeldt, S. Schafföner, M. Retsch, A. Greiner, G. Motz, S. Agarwal, *Sci. Adv.* **2023**, *9*, eade6066.